

Experimental Channel Characterization of Human Body Communication Based on Measured Impulse Response

Anna Vizziello, *Senior Member, IEEE*, Pietro Savazzi, *Senior Member, IEEE*, Renata Rojas Guerra and Fabio Dell'Acqua, *Senior Member, IEEE*

Abstract—Intra-body communication (IBC) will foster personalized medicine by enabling interconnection of implanted devices. Communication takes place through energy-efficient technologies such as capacitive coupling (CC) and galvanic coupling (GC); however, their modeling is still incomplete. This paper tackles characterization of the human body channel using impulse response, including a first-ever comparison of CC and GC in both wearable and implantable configurations. Experimental data are leveraged to evaluate the measured impulse response in ex-vivo chicken tissue and in-vivo human tissue in a frequency range up to 100 kHz. Pseudorandom noise (PN) sequences are transmitted in baseband and a correlative channel sounding system is implemented. Experimental results demonstrate that the channel is relatively flat in the frequency range of interest, thus offering the opportunity to simplify the design of an IBC transceiver. The relationship between the channel responses and the transmitter-to-receiver distance is also examined using linear correlation, and two regression models are developed. The results show that CC channels are not affected by distance within the range of investigation, while a negative relationship is found for GC channels. Finally, experiments reveal that implantable CC with isolated ground -not deeply investigated yet- is a very promising solution for IBC.

Index Terms—Wireless Sensor Networks, Intra-Body Communication, Intra-Body Networks, Human-Body Communication, Short Range Communications, Internet of Nano-Things, Internet of Medical Things, Body Area Networks, Coupling Technologies, Galvanic coupling, Capacitive Coupling, Experimental Testbed.

I. INTRODUCTION

Implantable medical devices will promote next-generation healthcare -including personalized medicine- through real-time physiological monitoring and proactive drug delivery, as envisioned in the fifth and beyond-fifth generation (5G/B5G) communication scenarios [1]. Challenging applications are conceived, such as recovery from paralysis and secure biometric data, which would require communication among implants for exchanging information between inside the body and outside it. These scenarios call for novel body-centric architectures, based on both intranet and Internet of Medical Things (IoMT) [2]–[5].

The intra-body network (IBN) paradigm enables interconnection of devices across the human body by enabling trans-

mission of acquired measurements among implanted sensor devices as well as to an external monitoring device. Suitable energy-efficient communication technologies are needed to implement this paradigm.

The most common intra-body communication (IBC) links use classical radio frequency (RF) waves at frequencies below 1GHz or in one of the standard Industrial, Scientific and Medical (ISM) bands, in the form of narrowband (NB) or ultra-wideband (UWB) signal [6]. However, several studies have demonstrated that RF signals, although profitably used for communication in on-body wearable devices, experience high losses within living tissues [7]. Consequently, the coverage is limited to short distances, plus possible heating may cause damage to the tissues conveying waves. Hence, other technologies have been explored as profitable alternatives for sub-cutaneous communication among implants. These include ultrasounds, capacitive coupling (CC) and galvanic coupling (GC) techniques, featuring lower attenuation within the human tissues compared to RF methods. Ultrasounds are acoustic waves showing good propagation properties in environments with high water content such as the human body [8]. However, they suffer severe multi-path fading and long delays caused by slow propagation; these factors can be counteracted by suitable design of transceivers, which however generally results into large sizes and high power consumption, unacceptable in implants. Considering the above context and related constraints, in this paper we investigate the so called coupling technologies for human body communication (HBC) that are capable of mitigating the above-mentioned issues. They consist of electromagnetic (EM)-based methods operating at low frequencies, up to 100 MHz.

Coupling technologies include capacitive and galvanic coupling methods [7], [9], and are already included in the Standard for Wireless Body Area Networks [10]. Capacitive and galvanic coupling rely on a couple of electrodes at the transmitter end and another one at the receiver end, although in a different configuration. CC is usually employed for wearable-type scenarios: only one transmitter electrode is attached to the body because the other one (i.e. ground electrode) is left floating. The same setup is used for the receiver [9]. Recently, preliminary explorations were made for implanted CC with an isolated ground electrode [11], [12]. In GC both the pairs of transmitter and receiver electrodes are attached to or implanted in the body [9]. These coupling technologies involve lower power levels compared to RF methods, enabling

Anna Vizziello, Pietro Savazzi, and Fabio Dell'Acqua are with the Department of Electrical, Computer and Biomedical Engineering, University of Pavia, Pavia, 27100 Italy (e-mail: name.surname@unipv.it), and with the Consorzio Nazionale Interuniversitario per le Telecomunicazioni - CNIT.

Renata Rojas Guerra is with the Departamento de Estatística, Universidade Federal de Santa Maria, Brazil (E-mail: renata.r.guerra@ufsm.br).

longer-distance transmission within the body, while at the same time avoiding tissue heating [9].

A. Research Motivation

In order to design proper transmission methods leveraging on these coupling technologies, an accurate channel model is essential for characterizing the electrical behavior of tissues. The standard approaches consist of quasi-static approximations [13], full wave numerical techniques, such as Finite Difference Time Domain (FDTD) Method, Finite Element Method (FEM) [7], [9] and Equivalent Circuit Analysis (ECA)-based models [7], [9], [14], [15].

The quasi-static field distribution analyses are computationally efficient, but they only model low frequency approximations to Maxwell's equations and can not be used for high-frequency applications [15]. Field analysis using FDTD and FEM are more accurate and flexible and recently, indeed, 2-D and 3-D models based on FDTD and FEM [16] were proposed to address realistic geometrical properties of the human body. These models, however, are computationally very demanding, making them unsuitable for rapid design and deployment of an IBN.

The ECA model offers a simple transfer function valid for a wide range of frequencies, with accurate and instantaneous gain computation; this makes it useful for IBN deployment in time-sensitive healthcare applications [15]. The methods developed consider a single layer of tissue or multiple heterogeneous layers composed of skin, fat, muscle, and bone tissues with experimental analysis [15].

These channel models are effective in representing the dielectric properties of human tissue that may affect signal propagation. On the other hand, they are unable to model essential properties of wireless channels, such as multi-path delay spread and amplitude fading statistics, that need to be taken into account when designing a communication system [17].

Methods based on impulse response show some potential for filling this gap, but, while this approach has been largely employed to characterize wireless channels over the air [18], limited effort has been spent so far to model IBC channels through impulse response methods [19]. Some studies were conducted only on CC in wearable configuration [20]–[23] and a few others on GC [17], [24]. However, a comparative investigation of both CC and GC technologies based on impulse response channel method, under both wearable and implantable configurations, has not been conducted yet, to the best of the authors' knowledge. The present work intends to address such research gap, thus enabling a more complete understanding - from the communication perspective - of the properties of each technology for the specific configuration. Furthermore, a linear correlation model and two regression models are proposed to investigate the relationship between the channel responses and the distance between the transmitter and receiver.

B. Main Contributions

The main contributions of this paper are the following:

- a channel model based on impulse response is derived for a comparison of CC and GC technologies. We explore and compare for the first time all the four possible configurations that include CC and GC in wearable and implantable scenarios.
- a first attempt is made to characterize the human-body channel using a correlative channel sounding method based on experimental measurements, conducted on both ex-vivo and in-vivo tissues, as an alternative to the standard ECA models, in order to capture the communication properties of the body channel.
- frequencies up to 100 KHz, which were only preliminarily evaluated in our previous work [24], are thoroughly investigated for the first time ever. The analysis of this frequency range is essential to developing a baseband UWB transceiver, whose simplicity is suitable for IBNs. In the future, our evaluation will be expanded to cover frequencies up to 100 MHz.
- safety considerations are incorporated in the employed experimental testbed by transmitting ultra-low power. Considered power levels are in the order of tens of μW , which mean negligible tissue heating. Extensive experiments were carried out and different distances between transmitter and receiver were tested.
- a linear correlation model and two regression models are proposed to verify the relationship between the channel responses and the distance between the transmitter and receiver for all the four configurations of GC and CC in wearable and implantable settings.

Interestingly, experimental findings indicate that the channel response is relatively flat for the frequency ranges of interest and the noise can be approximated as additive white Gaussian in all of the four considered electrodes configurations. These results allow to design simple transceivers, without complex receivers to counteract multi-path effects of the channel as required, for example, in ultrasound technology when employed for intra-body networks. The possibility to implement simple devices is fully in line with IBC requirements of energy-efficient solutions.

Furthermore, while it is well understood that CC outperforms GC in wearable settings, the state of the art (SoA) employs GC for implantable settings. A very interesting result obtained from the present work points at implantable CC with isolated ground as a promising solution for IBC. This technology has not yet been deeply investigated: only recently, some attention turned to CC in implantable configuration [11], [12], whereas previously it was usually employed in on-skin settings [9]. Comparing all possible configurations, we demonstrate that this version of implantable CC with isolated ground achieves lower attenuation levels. Hence, we believe that implantable CC may pave the way for interesting applicative developments in IBNs. However, implantable CC requires more complex hardware implementation due to the need for an isolated ground.

The rest of the paper is organized as follows. In Sec. II the considered low-power coupling technologies and their underlying physical principles are presented, together with configuration settings of the electrodes. Sec. III presents

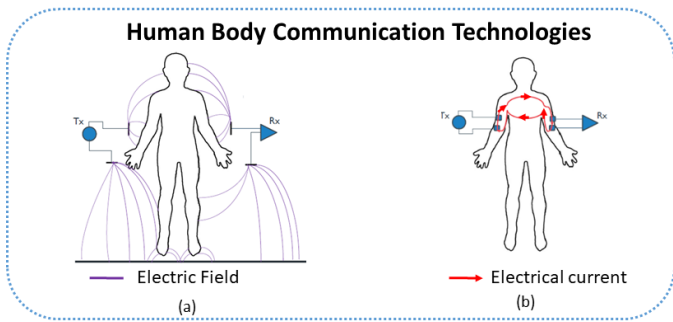


Fig. 1: Human Body Communication Technologies: (a) Capacitive Coupling (CC), (b) Galvanic Coupling (GC).

the channel model based on impulse response and Sec. IV describes the system overview and the experimental setup. Sec. V shows the experimental results, and Sec. VI closes the paper with some summarizing conclusions and future directions.

II. LOW-POWER COUPLING TECHNOLOGIES

Low-frequency EM technologies are customarily classified based on their coupling principles, that use different physical methods to generate an electrical signal to propagate through the human body. Body-area coupling methods are classified into capacitive and galvanic [25]. The electrical signal lies below 100MHz and conveys power levels in the order of μW , lower than those used in traditional RF signals, which extend up to several GHz [9], [26]. For this reason, body-area coupling methods have gained great attention in IBC research aimed at ensuring safety and decreasing energy consumption [27]. Indeed, on the one hand low levels of transmitted power ensure safety by avoiding heating of the body tissues as required by ICNIRP [28]. On the other hand, a low power consumption - in the order of few mW for both GC and CC [7] - assures longer battery life, as needed for IBN biomedical applications.

A. Coupling Technologies

Capacitive and galvanic couplings share some features as both employ electrodes to transmit and receive, albeit in different configurations. In CC, only one of the two transmitter electrodes is attached to the body while the other (ground) electrode is left floating. The same configuration is used for the receiver. The physical principle is based on near-field electrostatic coupling of the human body with its surroundings (Fig. 1(a)). The signal electrode of the transmitter induces the electric field in to the human body [9]. The induced electrical signal is controlled by an electrical potential and the body acts as a conductor with the ground as the return path [9]. The usual carrier frequency ranges from 100kHz up to 100MHz [9], [29] and this approach is usually employed in wearable scenarios covering long distances, up to 170cm. However, its operation may be affected by environmental conditions.

In GC, both pairs of electrodes, transmitting and receiving, are attached to or implanted in the human body. In GC, an AC current flows inside the body and the body acts as a

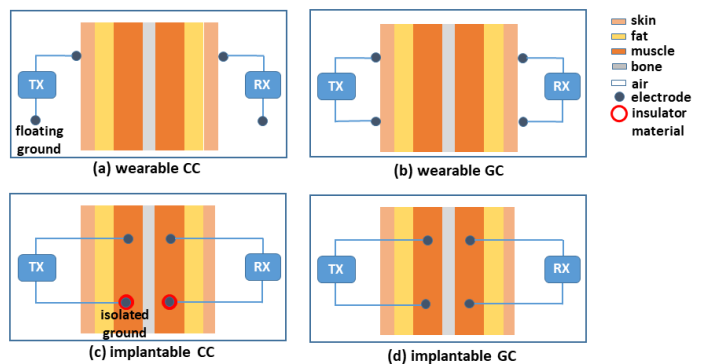


Fig. 2: Electrodes configuration placement for CC and GC technologies.

waveguide transmission line. Specifically, an electrical signal is applied differentially between the two electrodes of the transmitter. While the primary current carrying the data flows between the two transmitting electrodes, highly attenuated secondary currents can still be detected at the receiver electrodes (Fig. 1(b)). This technology is suitable for implanted scenarios and consumes two orders of magnitude less energy than RF transceivers [30]. Its usual operating frequency range is 1 kHz-100MHz with a coverage range up to 20–30cm [25].

In terms of applications, GC is usually employed for communication among devices in implanted scenarios, while CC is used for wearable settings to establish communication between on-body devices or with devices close to the body [11]. Anyhow, as it will be detailed in the following, a modified CC configuration has been recently proposed for implantable scenarios [11], [12], [31], [32].

B. Coupling Technology Configurations

Both coupling types require transceivers with two electrode pairs. Fig. 2 (a), (b) illustrates the different electrode configurations of CC and GC coupling in a wearable scenario. In CC, only one of the electrodes (signal electrode) of the transmitter side and receiver side is attached to the body, while the other electrode (ground electrode) floats (Fig. 2 (a)). In GC, both electrodes at transmitter and receiver side are attached to the human body [9] (Fig. 2 (b)). The different physical principle, explained above, calls for lower GC transmission rates and distances than those of CC. At the same time, there is no need for a floating ground reference nor for propagation outside the human body, hence GC does not suffer interference from external environment [7]. Anyway, given the aforementioned features, CC is the usual choice in wearable scenarios.

GC in implantable configuration consists of both electrode pairs of transmitter and receiver embedded inside the body as in Fig. 2 (d). So far, GC has been the preferred choice in implantable scenarios [11]. Recently, however, it has been demonstrated that a stable capacitive return path can be achieved not only by exposing the capacitive ground electrode directly to the air, as in wearable configurations, but also in implantable settings, provided that the ground electrode is isolated from human tissue [11] (Fig. 2 (c)). In this way, the path between transmitter electrodes has higher impedance than

the path to the receiver, resulting in reduced signal attenuation with respect to the implantable GC (Fig. 2 (d)). Therefore, the intra-body capacitive method emerges as a viable alternative for communication among implanted devices that can extend the transmission range currently achievable with GC technology. The results of implantable CC are very promising but this area is still in a nascent stage. Implantable CC is not widely accepted, also because a thorough investigation of its characteristics has not yet been carried out [12]. A few studies have been conducted, such as [11], [12], but a proper channel modeling for this configuration is still lacking, and further investigation is required to evaluate the features of implantable CC [12]. One of the objectives of the paper is hence to confirm the feasibility of this configuration and, at the same time, compare it with the implantable GC, due to the similarity of electrode configurations. The final goal is to build a first, comprehensive comparison among all the possible coupling wearable and implantable configurations, assessing benefits and drawbacks of each configuration. The investigation focuses on the impulse response of the communication channel.

III. CHANNEL MODELING BASED ON IMPULSE RESPONSE

This work uses a *stored channel impulse response* strategy [18], [33] to model the channel, which employs a correlative channel sounder. The method has been selected because of these two advantages: (i) the channel impulse responses measured and stored are based on experimental measurements, (ii) the stored responses are reproducible and reusable, which is useful when simulating and optimizing communication systems. Before detailing the developed channel model, the theoretical foundations of CC and GC are recalled in the following sub-section.

A. Dielectric Properties of Human Tissues

Gauss's law and charge-continuity equations are reported below as eqs. (1) and (2):

$$\nabla \cdot D = \rho \quad (1)$$

$$\nabla \cdot J = \nabla \cdot (\sigma E + J_{source}) = -\frac{d\rho}{dt} \quad (2)$$

in which D is the electric displacement, ρ is the electric charge density, J is the current density, σ is the electrical conductivity, E is the electric field intensity and J_{source} is the current density of the source.

When the product of body size and the wave number in biological tissues is much larger than 1, wave propagation and inductive effect in biological tissues may be neglected [12], [34]. Therefore, Maxwell's equations can be decoupled as quasi-static electric field governing equation:

$$\nabla \cdot (j\omega\epsilon\nabla V) + \nabla \cdot (\sigma\nabla V) + \nabla \cdot J_{source} = 0 \quad (3)$$

in which V is the electric potential, ω is the angular frequency, and ϵ is the permittivity.

The permittivity ϵ is governed by the Cole–Cole equation, which shows how the dielectric properties of a tissue change over a broad frequency range [9]:

$$\hat{\epsilon}(\omega) = \epsilon_\infty + \frac{\Delta\epsilon}{1 + (j\omega\tau)^{(1-\alpha)}} \quad (4)$$

where $\hat{\epsilon}$ is the complex relative permittivity, and $\Delta\epsilon$ is the magnitude of the dispersion calculated as $\Delta\epsilon = \epsilon_s - \epsilon_\infty$, in which ϵ_∞ is the permittivity at field frequencies where $\omega\tau \gg 1$ and ϵ_s the permittivity at $\omega\tau \ll 1$. τ is the relaxation time constant that depends on physical processes, such as ion effects, and α is a distribution parameter that lies between 0 and 1 [9] and is a measure of the broadening of the dispersion. The properties of a tissue are therefore more appropriately described by means of multiple Cole–Cole dispersion:

$$\hat{\epsilon}(\omega) = \epsilon_\infty + \sum_n \frac{\Delta\epsilon_n}{1 + (j\omega\tau_n)^{(1-\alpha_n)}} + \frac{\sigma_i}{i\omega\epsilon_0} \quad (5)$$

where σ_i is the static ionic conductivity and ϵ_0 is the permittivity of free space. Equation (5) may be used to predict the dielectric behaviour in the considered frequency range, with a proper choice of parameters for each tissue.

The complex conductivity and the complex specific impedance of a tissue may be then calculated as [9]:

$$\hat{\sigma} = j\omega\epsilon_0\hat{\epsilon}, \quad \hat{z} = \frac{1}{\hat{\sigma}} \quad (6)$$

Electrical properties of human body tissues may be modeled by equivalent electrical components such as resistors and capacitors. Such properties also represent the building bricks in developing the transfer function of the body channel based on a circuit model, a FEM, or a circuit-based FEM model [9]. Alternatively, given the dielectric properties of the human tissues, we leverage a different approach based on channel impulse response. This method is more suitable to analyze the properties of the body channel from a communication perspective. In the rest of this paper, the term *channel* refers to *human body channel*.

B. Correlative Channel Sounders

A channel sounding signal is composed of a pulse transmission that occurs with predetermined repetition intervals. When signals are received, a sounder device filters and records them for off-site storage and processing [17]. The type of sounding signal sent depends on the method used [33] and in the following we consider pseudorandom noise (PN) sequences.

As is known, the received signal can be described as $y(t) = x(t) * h(t) + n(t)$, where $x(t)$ and $y(t)$ are the transmitted and received signal, respectively, $h(t)$ is the channel impulse response, $n(t)$ is the additive white noise, and $*$ is the convolution operator. Correlating each side of the previous equation with $x(t)$ yields:

$$R_{xy}(\tau) = h(\tau) * R_{xx}(\tau) \quad (7)$$

where R_{xy} is the cross-correlation function between $x(t)$ and $y(t)$, $R_{xx}(\tau)$ is the auto-correlation function of $x(t)$, τ is the delay time. $n(t)$ and $x(t)$ are assumed uncorrelated.

The impulse response $h(t, \tau)$ is expressed as a function of time t and delay τ . However, if the channel impulse response $h(t, \tau)$ changes slowly within the time interval required to measure the correlation function, we may assume a time-invariant impulse response $h(\tau)$. Then (7) can be employed to measure $h(\tau)$. This can be achieved if R_{xx} approaches a delta function, as in this case R_{xy} becomes a good approximation of the channel impulse response (CIR) $h(\tau)$ as shown in (7). To this aim, PN sequences are used as the transmitted signal $x(t)$ since they yield an auto-correlation function with a high correlation peak and much lower off-peak components [18].

The use of maximal-length PN sequences as the transmitted signal leads to an auto-correlation function a high correlation peak and extremely low side lobes (high peak-to-off-peak ratio). This feature allows any multi-path component to be detected at the receiver when correlating the channel output with the originally transmitted PN sequence by means of a convolution matched filter [24]. Fig. 3 illustrates the blocks of the considered channel sounding architecture.

The power delay profile $P_h(\tau)$ can be calculated by squaring the impulse response without averaging over time:

$$P_h(\tau) = |h(\tau)|^2 = |R_{xy}(\tau)|^2 \quad (8)$$

The signal loss and power delay profiles of the conducted measurements may be used to obtain the following channel parameters: mean signal loss, mean delay, root-mean-square (rms) delay, received power, coherence bandwidth.

The mean signal loss is calculated by averaging the magnitudes of the signal loss at all frequencies, while the mean delay $\bar{\tau}$ and rms delay σ_τ are obtained using the power delay profile:

$$\bar{\tau} = \frac{\sum_{k=1}^{N_I} \tau_k P_h(\tau_k)}{\sum_{k=1}^{N_I} P_h(\tau_k)} \quad (9)$$

$$\sigma_\tau = \sqrt{\frac{\sum_{k=1}^{N_I} (\tau_k - \bar{\tau})^2 P_h(\tau_k)}{\sum_{k=1}^{N_I} P_h(\tau_k)}} \quad (10)$$

where $N_I = N_{PN} * N_s$ with N_{PN} being the number of PN bits and N_s number of samples per bit.

The coherence bandwidth B_c may be calculated using a frequency correlation function [35] expressed as a function of the power delay profile [21], [35]. Given the inverse relation between B_c and σ_τ , the coherence bandwidth B_c can be calculated from σ_τ [35].

C. A Linear Regression Model for the Channel

To achieve a better understanding of the channel features, we performed a correlation analysis and constructed a linear regression model to examine the relationship between the CIR and the distance between the transmitter and receiver d_{tx-rx} .

Δ_p is defined as the maximum peak-to-peak amplitude of the cross-correlation $R_{xy}(\tau)$ in the time domain, i. e., $\Delta_p = \max(R_{xy}(\tau)) - \min(R_{xy}(\tau))$. Let $\{(\delta_{p;i}, d_{tx-rx;i}), \dots, (\delta_{p;n}, d_{tx-rx;n})\}$ be a paired sample of size n , where $\delta_{p;i}$ is the observed Δ_p and $d_{tx-rx;i}$ is the distance between transmitter and receiver for the i th measure

in the sample, $i = 1, \dots, n$. The Pearson coefficient is used to assess a possible linear correlation between these variables:

$$r = \frac{\sum_{i=1}^n (\delta_{p;i} - \bar{\Delta}_p)(d_{tx-rx;i} - \bar{d}_{tx-rx})}{\sqrt{\sum_{i=1}^n (\delta_{p;i} - \bar{\Delta}_p)^2} \sqrt{\sum_{i=1}^n (d_{tx-rx;i} - \bar{d}_{tx-rx})^2}} \quad (11)$$

where $\bar{\Delta}_p$ and \bar{d}_{tx-rx} are the sample means of Δ_p and d_{tx-rx} , respectively. The value of r ranges from -1 to 1, with its sign indicating the direction of the relationship, and no linear dependency between the variables marked by $r = 0$. Therefore, we perform a hypothesis test to verify if the Pearson correlation is statistically equal to zero. The test statistic is based on Student's t -distribution with $n-2$ degrees of freedom, under the null hypothesis that the samples follow independent normal distributions. It holds approximately in case of non-normal observed values if sample sizes are large enough.

Moreover, in case of a linear relationship between Δ_p and d_{tx-rx} , as verified in Sec. V-B, it is possible to construct a linear regression model to compute the marginal effect of d_{tx-rx} over Δ_p values. We perform the analysis using two different approaches. In the first approach, we assume that the value of Δ_p can be represented by a simple linear regression using d_{tx-rx} as a continuous predictor. In other words, we assume it is possible to develop the sample regression line in its stochastic form as follows:

$$\delta_{p;i} = \hat{a} + \hat{b} d_{tx-rx;i} + \hat{\epsilon}_i, \quad i = 1, \dots, n \quad (12)$$

where \hat{a} is an estimator of the mean of Δ_p value when the $d_{tx-rx;i} = 0$, \hat{b} is an estimator of the expected change in the Δ_p when the distance increases by one unit, and $\hat{\epsilon}_i = \delta_{p;i} - (\hat{a} + \hat{b} d_{tx-rx;i})$ is the residual term.

In the second approach, dummy variables are created to compute the differences in the Δ_p for each measured distance. Considering the experiment that evaluates Δ_p for three distances d_0, d_1 and d_2 , we define two dummy variables to be employed as predictors in a multiple regression model, using d_{tx-rx} equal to d_0 as the base category. Therefore, the second approach assumes a multiple regression model according to the following equation for its stochastic form:

$$\delta_{p;i} = \hat{a} + \hat{b} d_{1;i} + \hat{c} d_{2;i} + \hat{\epsilon}_i, \quad i = 1, \dots, n \quad (13)$$

where \hat{a} represents an estimator of the mean Δ_p value when $d_{tx-rx} = d_0$, \hat{b} is an estimator of the mean Δ_p when d_{tx-rx} changes from d_0 to d_1 ($d_{tx-rx} = d_1$ and $d_{1;i} = 1$), \hat{c} is an estimator of the mean of Δ_p when the distance changes from d_0 to d_2 ($d_{tx-rx} = d_2$ and $d_{2;i} = 1$), and $\hat{\epsilon}_i = \delta_{p;i} - (\hat{a} + \hat{b} d_{1;i} + \hat{c} d_{2;i})$ is the residual term.

We use the ordinary least squares method to estimate the regression coefficients in (12) and (13). Additionally, we examine their residuals as a diagnostic tool. Since the linear regression relies on the assumption that the residuals follow a normal distribution with mean equal to zero and constant variance [36], we perform the Shapiro-Wilk (SW) test [37] to examine the normality hypothesis for the regression residuals. Its null hypothesis is that the residuals are normally distributed. Therefore, normality can be assumed if its p -value is larger than 0.05.

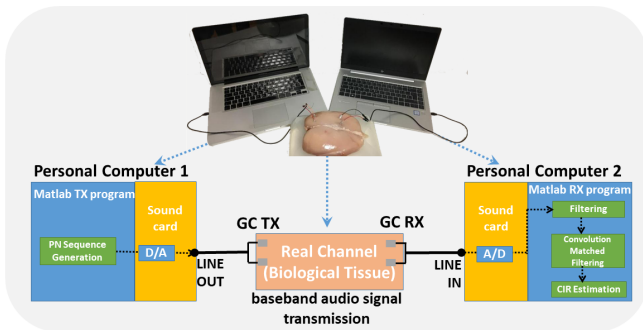


Fig. 3: Block diagram of the Correlative channel sounding system.

We also evaluate the adjusted-R-squared (\bar{R}^2), which is defined as follows:

$$\bar{R}^2 = 1 - \frac{(n-1) \sum_{i=1}^n \hat{\epsilon}_i^2}{(n-p) \sum_{i=1}^n (\delta_{p,i} - \bar{\Delta}_p)^2} \quad (14)$$

where p is the total number of explanatory variables in the model, and n is the sample size. The \bar{R}^2 indicates the proportion of the variance in the response variable that can be explained by the predictor variables in the model. Therefore, it can be used as a measure for how well each model fits, to select the most suitable. As detailed in Sec. V-B, experimental results reveal that -within the considered distances- a linear relationship between Δ_p and d_{tx-rx} exists for GC but not for CC.

IV. EXPERIMENTAL SYSTEM OVERVIEW

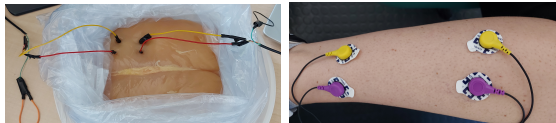
A. Testbed Description

In order to experimentally measure the channel impulse responses, PN sequences were transmitted in baseband. A linear polynomial PN sequence of degree $m = 14$ was built using a linear-feedback shift register with a chip duration of $5.2 \mu s$ (corresponding to a bandwidth of 96 kHz) as in [24]. These parameters were set according to the frequency range employed in the test system, up to around 100 KHz.

The testbed [38] was modified to implement a correlative channel sounding, only explored to a limited extent in our previous work [24] (Fig. 3). The source code of the transceiver [38] is available online on Code Ocean for sake of replicability [39]. Hardware requirements are moderate, limited to two PCs with sound cards used to generate/transmit and receive the signal in a subset of the GC frequency range [38]. As shown schematically in Fig. 3 and better detailed in Fig. 4(a), we used two PCs as transmitter/receiver and secured common ground isolation between them, as required by coupling technologies [38], [40]. Specifically, a battery-powered laptop was employed as the transmitter (TX) and a desktop PC as the receiver (RX), respectively (Fig. 4(a)). The laptop was unplugged from the grid to avoid common ground return paths between the transmitter and the receiver. A Matlab session



(a) Implemented coupling-based testbed



(b) Electrodes implanted configuration with ex-vivo biological tissue (c) Electrodes wearable configuration with in-vivo biological tissues

Fig. 4: Implemented coupling-based testbed and electrodes placement.

TABLE I: Parameters setting

Parameter	Value
PN sequence degree m	14
Bandwidth (kHz)	96
Waveform sampling frequency f_{sa} (KHz)	192
Sequence length N (# of symbols)	100000

had to be kept open and active on each machine, to run the transmitter and receiver software, respectively.

The generated PN sequences were transmitted using the tx Matlab program, and then converted from digital to analog (D/A) domain to be sent over the sound card of the transmitter (see Fig. 3). The transmitted signal is injected into the biological tissue through a cable connected to the $LINE OUT$ jack on one side and to the two transmitter electrodes on the opposite side.

After transmission, the two electrodes of the receiver detected the received signal, which was then delivered to the second computer via a cable connected to the $LINE IN$ jack. The Matlab rx program includes a 50 Hz filter and a convolution matched filter to correlate the channel output with the transmitted PN sequence known at the receiver, to build the CIR estimation (Fig. 3). The audio frequency sampling f_{sa} was set to 192 KHz, with 16 bits per sample. Table I shows the values of the main system parameters. Some of these latter, such as the polynomial degree of the PN sequence, may be set in the tx/rx Matlab program code, while other audio parameters can be set through the control panel of each computer. In particular, at the TX computer, one of the two channels (either left or right) had to be muted, and some audio features disabled, such as audio optimization, while at the RX computer, DC compensation had to be disabled.

B. Experimental setup

In our experiments, we considered two configurations: one with electrodes implanted in *ex-vivo* chicken breast tissue (Fig. 4 (b)) and another one with wearable electrodes placed on *in-vivo* human skin (Fig. 4 (c)). Indeed, given the human-like dielectric properties of chicken and pork muscle tissue [41], [42], we decided to use chicken breast for the implantable setup. Electrodes with different sizes (0.5 mm and 1 cm diameter) were tested.

For the case of *ex-vivo* tissue we employed low-cost regular leads, covered with an aluminum foil to avoid oxidation due to the water content of the chicken breast. We used small-sized circle electrodes (in the order of 0.5 mm diameter) to test a real configuration scenario for future miniaturized medical devices. For the case of *in-vivo* tests we employed commercial electrodes with a size of 1 cm, applied on human leg skin. The *ex-vivo* tissue, a sample of chicken breast sized roughly 21 cm × 16 cm × 6 cm, consisted of a single-layer tissue, i. e., the muscle. The *in-vivo* tissue (human leg) involved heterogeneous multi-layers tissues, i. e., skin, fat, muscle and bone tissues. Indeed, although the electrodes are placed on the skin, the signal is expected to flow not only in the outmost layer of skin but rather in all of the aforementioned tissues [25]. Performances were computed by averaging over 100 measurements. The measurements were carried out over a period of several days, under the same conditions and for the same subject as *in-vivo* tests. Measurements on the *ex-vivo* chicken were conducted on the same meat only for two consecutive days to avoid deterioration of the meat, and consequent spurious drifts in dielectric properties [43]. The experiments were then repeated on ten different chicken breasts and ten human subjects. The transmission power P_{Tx} was in the order of 10 μW . It was calculated by measuring the potential difference at the output of the transmitter device with a voltmeter in parallel and measuring the current with an amperometer in series under the hypothesis of the impedance characteristics in [44]. A different transmission power can be set by varying the audio volume of the transmitter device. The signal-to-noise ratio (SNR) was in the order of 20 dB, and the inter-electrodes distance at both transmitter and receiver side was set to 1.5 cm for *ex-vivo* and 4 cm for *in-vivo* experiments, while the transmitter-to-receiver distance was varied during the tests. The inter-electrodes distances of 1.5 and 4 cm were found -by experiment- to be a good compromise: shorter distances imply the loop of injected primary current is too short to propagate any secondary current [45], whereas longer distances enlarge the size of the device, not recommended for medical applications [15]. As shown in Table II, a CFR magnitude around 4 dB higher was found when increasing the inter-electrode distance in GC implantable configuration from 1.5 to 4 cm. The difference was less evident in the wearable GC setting: only around 1 dB from 4 to 8 cm inter-electrode distance. On the contrary, the differences were negligible for CC. Similar results were obtained when increasing the size of the electrode. For example, 4 dB CFR magnitude change was found in GC wearable configuration when varying the electrode diameter from 0.5 to 1 cm.

TABLE II: Inter-electrode distance evaluation with fixed $d_{Tx-rx} = 14$ cm.

Experiment	d_{int} (cm)	CFR (dB)
Implantable GC	1.5	34.02
Implantable GC	4	38.27
Wearable GC	4	38.78
Wearable GC	8	39.82
Implantable CC	1.5	77.1
Implantable CC	4	77.2
Wearable CC	4	72.03
Wearable CC	8	72.13

V. EXPERIMENTAL CHANNEL CHARACTERIZATION

The received signals were post-processed in MATLAB to obtain the channel impulse response (CIR) and channel frequency response (CFR) for both GC and CC technologies in wearable and implantable configurations.

Preliminary evaluation demonstrated that the GC-based communication channel is non-frequency-selective [17], [46], although this was proved only in wearable setting. In other studies [21], [47]–[49], some aspects of the CC channel were presented. In [21] a channel delay spread was evaluated, which however was not due to the multipath effects as in radio channels, but rather to capacitive coupling effects in the body. The spreading time resulted to be constant as in a resistor–capacitor circuit [21]. However, in these studies the transceiver setup considered a transmitter and/or receiver sharing an Earth ground connection through the power grid. This means characterizing a channel which is in fact different from the real case of wireless body area network (WBAN) or intra-body network, which lacks any common ground. Furthermore, these papers did not consider nor compare the four possible configurations discussed in this paper and shown in Fig. 2, since the evaluation of impulse response was conducted only in wearable settings and separately for GC and CC [17], [21], [46]–[49]. Moreover, the frequency range was different from the considered one, up to 100 KHz. The evaluation of this frequency range will allow to design baseband UWB transceiver, whose simplicity matches well the requirements of long-lasting implants in IBNs.

Fig. 5 illustrates the measured CIR for the communication scenario of heterogeneous tissues, i.e. the *in-vivo* tissues of a human leg. The figure shows the high peak-to-off-peak ratio discussed in Sec. III, which provides good correlation results from the experiments. All the CIRs obtained in different scenarios show a similar behaviour, suggesting no multi-path effect in the body channel at the considered frequencies.

A. Experimental Results

Figs. 6 and 7 represent the CIR and its corresponding frequency domain representation, i. e., the CFR, for implanted and wearable scenarios with tx -to- rx distances of 6 cm and 10 cm, respectively. Similar trends with different magnitudes for channel gain are obtained in the CFRs while changing distances between transmitting and receiving electrodes, as detailed in Fig. 8.

The CFRs in Figs. 6 and 7 indicate that the channel is relatively flat within the frequency range of interest, although with lower channel gain for the GC than for the CC technology. In

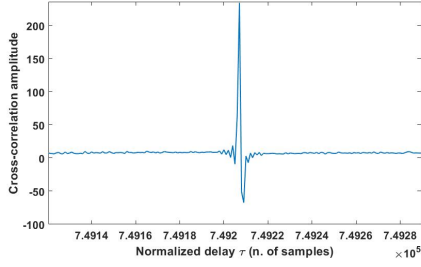


Fig. 5: Channel Impulse Response (CIR) for a wearable GC configuration in heterogeneous *in-vivo* biological tissues with 1 cm electrodes, $d_{int} = 4$ cm inter-electrodes distance, and $d_{tx-rx} = 10$ cm distance between transmitter and receiver.

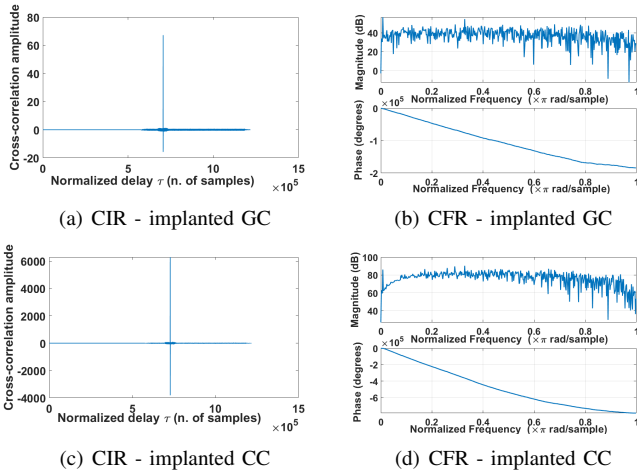


Fig. 6: The measured channel impulse response (CIR) and channel frequency response (CFR) in implanted configuration with 0.5 mm electrodes size and $d_{tx-rx} = 6$ cm with *ex-vivo* biological tissue. The inter-electrodes distance is set $d_{int} = 1.5$ cm for both GC and CC configurations. Note that the ground is isolated at both transmitter and receiver in implanted CC configuration.

particular, focusing on the implantable setting shown in Fig. 6, the CC method shows a higher peak-to-off-peak ratio for CIR compared to GC technology (Fig. 6 (a) vs. Fig. 6 (c)), as well as larger CFR magnitude, around 76 dB vs. 36 dB (Fig. 6 (b) vs. Fig. 6 (d)). These results prove the great potentials of implantable CC with isolated ground. So far, the SoA focused on CC with floating ground electrodes for wearable configurations, and on GC for implantable settings. However, as reported in Fig. 6 (b) and (d), this new version of CC with isolated ground can achieve a CFR magnitude 40 dB higher than GC in implantable configuration, starting from the same transmitted power. This makes it possible to operate on longer transmission distances for implantable CC than GC. Confirming clues were then found in very recent literature [11], [12], [31], [32].

Fig. 8 shows the mean and standard deviation as descriptive measures of CFR value for CC and GC technologies in both implantable and wearable configurations while varying the distance d_{tx-rx} . The maximum distance d_{tx-rx} for *in-vivo*

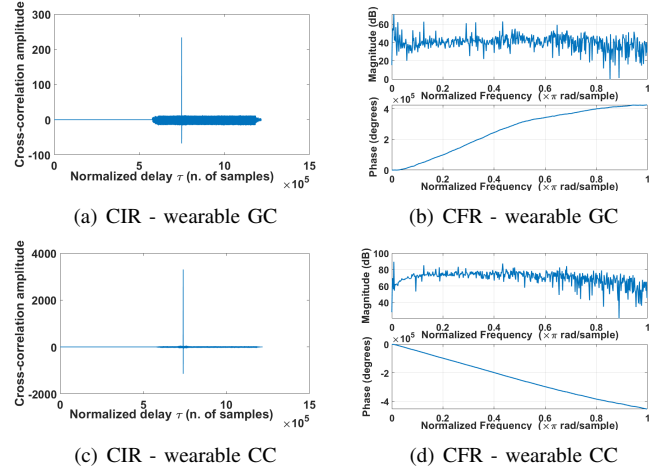


Fig. 7: The measured channel impulse response (CIR) and channel frequency response (CFR) in wearable configuration with 1 cm electrodes size and $d_{tx-rx} = 10$ cm with *in-vivo* heterogeneous biological tissue. The inter-electrodes distance is set $d_{int} = 4$ cm for both GC and CC configurations. Note that the ground is floating at both transmitter and receiver in wearable CC.

setting was set to 30 cm, while it was constrained to 14 cm for *ex-vivo* by the size of the chicken breast. The mean CFRs are represented along with their standard deviations. CC technology always achieves better performance with higher CFR than GC. Fig. 8 shows that CC, unlike GC, does not depend strongly on channel length d_{tx-rx} , showing similar CFR values as the distance increases. Indeed, as detailed in Sec. V-B, a linear relation between the peak-to-peak of the CIR and d_{tx-rx} was found for GC but not for CC within the considered distances. As shown in Fig. 8, the GC dependency with distance is less evident for distances longer than 25 cm, which may be due to the marginal signal propagation effects from the body into the surrounding [15], that can externally reach the receiver. It is worth noting that higher CFR values were found for CC even for distances much longer than those applied in GC. Similar findings were obtained in [45], and in [50] where several measurements on diverse subjects were performed.

Figs. 9 and 10 show the mean amplitude of the received signal in time, normalized to the number of bits of the ADC converter, the maximum peak-to-peak amplitude of the cross-correlation in time, and the mean amplitude of the cross-correlation in frequency, for implantable and wearable scenarios, respectively. Values were averaged over 100 measurements. As mentioned above, the value of maximum distance in Figs. 9 and 10 was constrained by the size of the chicken breast. The same value was considered also for the *in-vivo* tests with a human leg for comparison purposes, although a really fair evaluation of the differences is not possible because electrode sizes and biological tissues were different. Nevertheless, comparing the two figures, it is possible to note that the amplitude of the received signal is lower for GC in implantable configuration than in wearable scenario (Fig. 9(a))

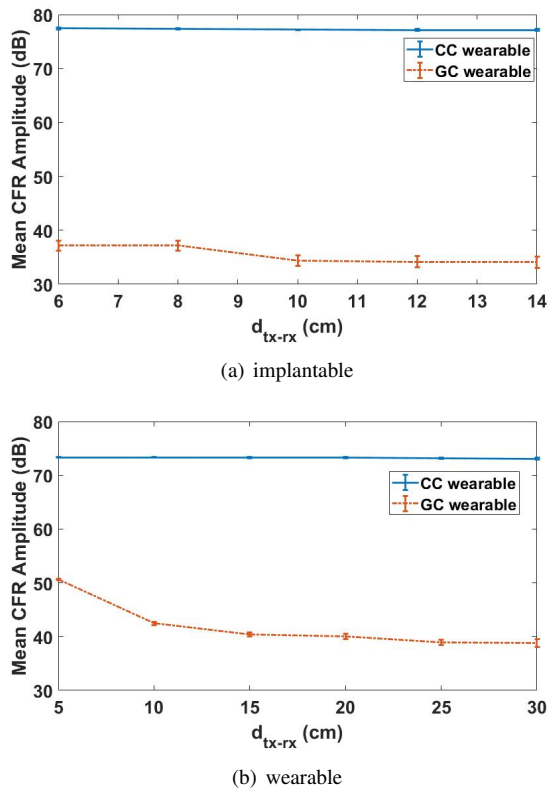


Fig. 8: Comparison between the CFR magnitude for different tx -to- rx distances (d_{tx-rx}). The mean and standard deviation of CFR magnitude are represented for CC and GC in implantable and wearable configurations. 0.5 mm electrodes are employed with *ex-vivo* tissue and 1 cm electrodes for *in-vivo* heterogeneous tissues.

vs Fig. 10(a)). However, cross correlations in both time and frequency domains are better for GC in implantable than in wearable scenario (Fig. 9(b) vs Fig. 10(b), and Fig. 9(c) vs Fig. 10(c)). This is due to a larger electrode size in wearable configuration -1 cm vs 0.5 mm of implantable setting- that allows higher signal amplitude at the receiver with, however, stronger noise also (see Fig. 7(a) vs Fig. 6 (a)). During the experiments, it was not possible to compare different electrode sizes in implantable and wearable configurations for feasibility reasons. Indeed, implantable and wearable configurations in the chicken breast showed similar results due to the single layer tissue, while human implantation was not explored since it would have required appropriate medical lab facilities. Overall, Figs. 9 and 10 show better performances for CC over GC. Indeed, referring to Fig. 9 for implantable setting, all the considered performance parameters are higher for CC with respect to GC, i. e., the mean amplitude of the received signal in time (Fig. 9 (a)), the maximum peak-to-peak amplitude of the cross-correlation in time (Fig. 9 (b)), and the mean amplitude of the cross-correlation in frequency (Fig. 9 (c)). The parameters in the time domain (Fig. 9 (a)-(b)) show larger differences than in the frequency domain (Fig. 9 (c)). The same trend is evident for wearable settings in Fig. 10, although with a smaller difference between CC and GC than in implantable

configuration. However, it is worth noting that in wearable configuration, CC may suffer from external interference. This is due to its physical principle based on the formation of an electrical field around the body, whereas in GC fields and currents are confined inside the body. Summarizing, while results of Fig. 10 for wearable configurations were expected being CC preferred to GC according to SoA, up to now GC was the only available choice for implantable setting. Anyhow, the experiments (Fig. 9) revealed the superiority of the new version of implantable CC with isolated ground. Moreover, the latter has also great potential in terms of miniaturization compared to the other coupling technologies, as detailed in Sec. VI.

In addition to the above, the results of experiments conducted over ten different subjects are presented in Fig. 11, which summarizes the mean and standard deviation of the distances. A dependency on the subject was found in terms of CFR magnitude, although the flat behaviour was maintained over the frequency range of interest. Indeed, it is possible to observe a larger standard deviation in Fig. 11 than in Fig. 8(b) that was referring to a single subject - as an example for GC configuration at $d_{tx-rx} = 5$ cm, the standard deviation was 5 dB in Fig. 11 while only 0.34 dB in Fig. 8(b). This is due to the different hydration and diameter of the subject's leg, as has also been reported by other works [21], [45], as well as different thickness of the tissues. However, the difference for CC was smaller than for GC, which can be explained by the fact that CC is not as influenced by the human body as it is by the CC return path in the environment, through which the signal loop is closed. On the contrary, the GC physical principle of weak secondary currents flowing in the body makes the technology more dependent on the body channel. Differences between chicken breasts were less evident, which may be due to the similar size of the selected meat and limited variability of the tissue. Further analysis are being planned for *ex-vivo* chicken which will include heterogeneous tissues, like bones, muscle fat and skin, to evaluate the related variability effects.

Finally, a preliminary evaluation of the impact of limb motion has been conducted under two configurations. In the first one, the transmitter and the receiver were placed on the same calf with a d_{tx-rx} distance equal to 15 cm and the experiments did not show changes in the CFR while moving the leg. In the second configuration, the transmitter and receiver were located on the opposite side of the elbow, hence a relative motion occurred between them when moving the arm, and even in this case the CFR did not show relevant changes. These findings are in line with the expected results; when the coherence time is much larger than the symbol time, a channel may be considered slowly time-variant. This condition is easily met by commonly-used IBC symbol rates against regular body movement speeds [51], [52].

B. Analysis of the Linear Regression Model

As mentioned in Sec. III-C, for each experimental setup, i. e., GC and CC in both wearable and implantable configurations, we analyzed the relationship between Δ_p and d_{tx-rx}

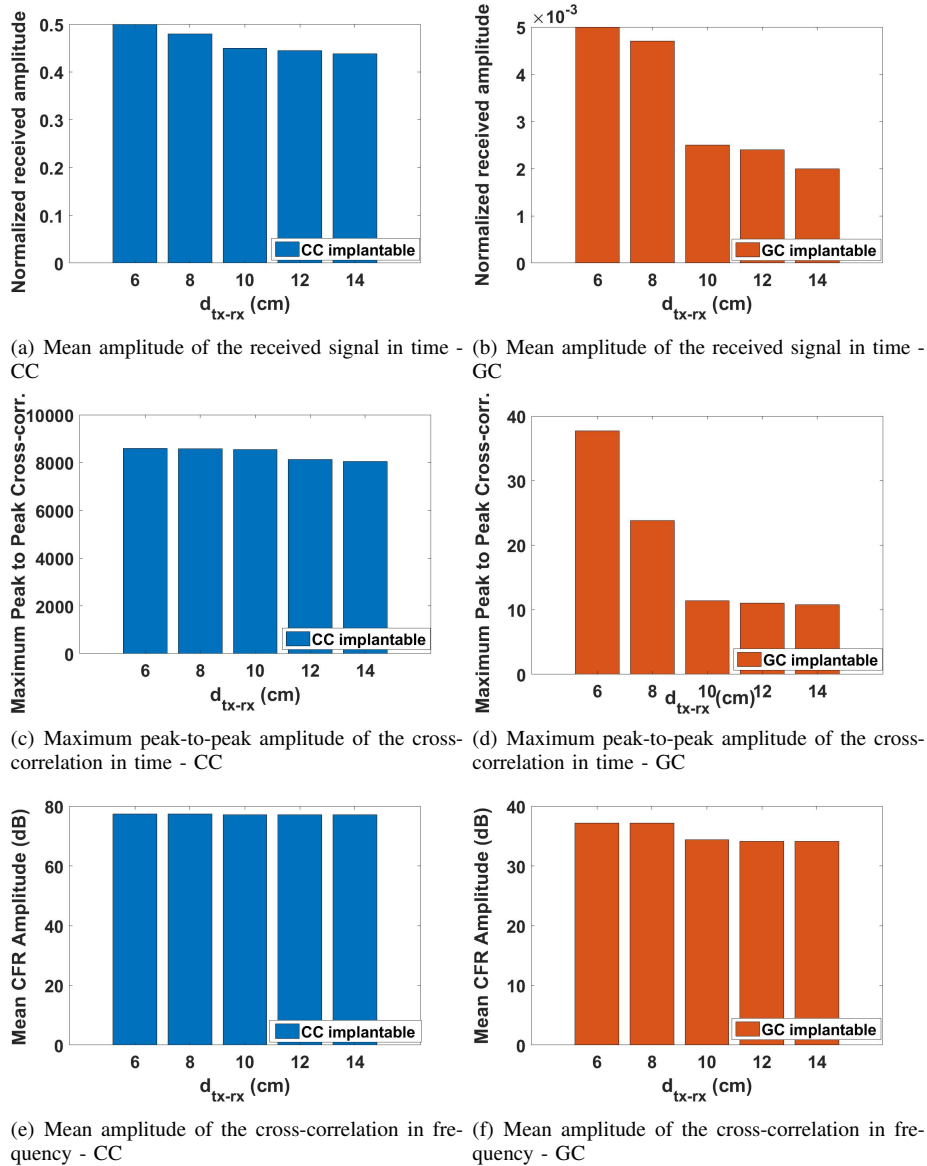


Fig. 9: Comparison between GC and CC in implanted configuration for different tx -to- rx distances (d_{tx-rx}). In this case, 0.5 mm electrodes are employed on *ex-vivo* tissue.

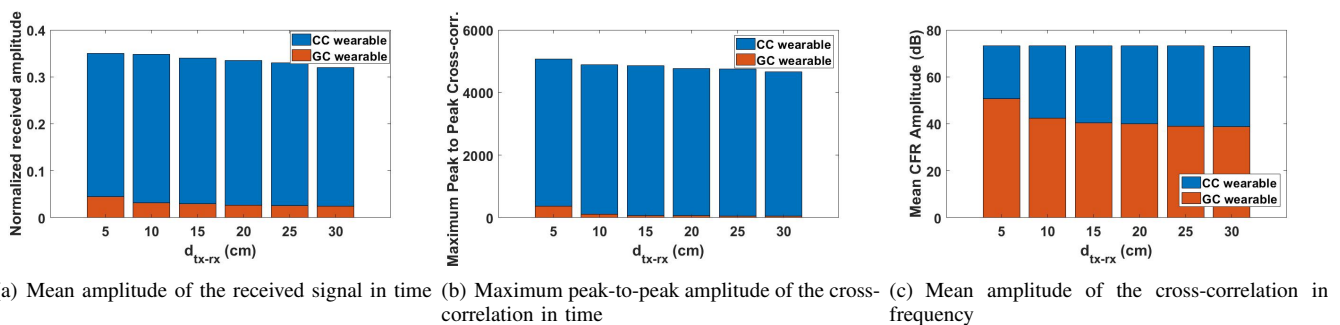


Fig. 10: Same as fig. 9, for wearable configuration and 1 cm electrodes on *in-vivo* heterogeneous tissues.

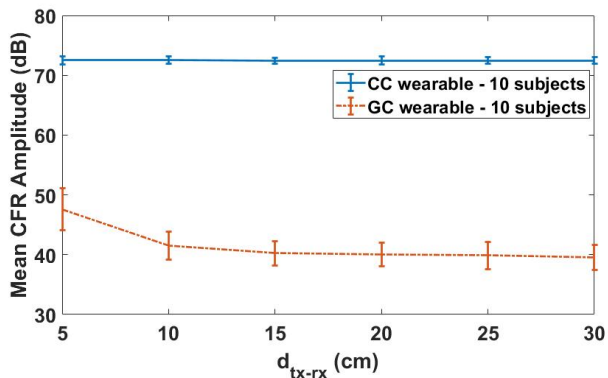


Fig. 11: CFR for wearable configurations in heterogeneous *in-vivo* biological tissues for ten subjects with 1 cm electrodes, $d_{int} = 4$ cm inter-electrodes distance, and different distances d_{tx-rx} between transmitter and receiver.

by computing the Pearson correlation and verifying if it was statistically significant. The results in Table III show negative coefficients for all cases, indicating that Δ_p decreases as the distance increases. However, the correlation is significant at the 5% significance level only for the GC channel since the p-value is < 0.01 in both implantable and wearable GC setups. Pearson correlation statistically equals zero for the CC channel in implantable and wearable configurations.

Table IV reports results obtained by fitting the regression models in (12) and (13), corroborating the correlation analysis. Indeed, Table IV shows that only the GC channel presents significant values for the coefficients related to the distances and satisfies the normality assumption for the residuals (p-value of the SW test over 0.05). Therefore, the regression coefficients within the considered distances can be interpreted only for results regarding the GC technology. Similar findings were obtained in [45] and in [50].

From the first approach for implantable GC, i. e., a linear regression using d_{tx-rx} as a continuous predictor (see Sec. III-C), we obtain the mean Δ_p value equals 127.99 when the distance is zero and decreases by -9.04 for every unit increase in the distance. Regarding wearable GC, the mean Δ_p value is around 374.31 when the distance is zero, with a 95% confidence interval (IC95%) of (348.64,399.98) and a marginal effect of -7.62 for a unit increase in the distance, IC95% of (-9.75,-5.48). The cross-correlation values were not normalized, while the considered sequences had the same length and energy in the same transmission conditions.

The second approach, which considers dummy variables in the regression model (see Sec. III-C), offers a different interpretation. It compares the mean Δ_p value (\hat{a}) at 6 cm distance with the longer distances considered in each experimental setup (10 and 14 cm for implantable setup, 10 and 20 cm for wearable setup). Regarding the implantable GC configuration, \hat{b} indicates that increasing the distance from 6 cm to 10 cm, on average, reduces the Δ_p by -54.4, and IC95% by (-73.03,-35.77). From this result, we can calculate the mean Δ_p value for a distance of 10 cm, which gives 25.4 cm. Analogously, the mean Δ_p value decreases by -68.3, and

IC95% by (-89.82,-46.78), when the distance increases from 6 cm to 14 cm, resulting in a mean value of 11.5 for the latter case. Notice that \bar{R}^2 is higher for this approach. Therefore, in implantable GC configuration, the proportion of the variance in the Δ_p is better explained by the model in (13).

When analyzing the wearable GC configuration, the model in (12) appears to be more suitable based on its better goodness-of-fit measure. Indeed, it returns a higher value of \bar{R}^2 , besides \hat{b} is not significant under the second approach. Therefore, we analyze the mean Δ_p values using coefficients estimated for the model in (12). By doing this, the Δ_p fitted values are given by $\hat{\delta}_{p;i} = 374.31 - 7.62 d_{tx-rx;i}$. In this case, we obtain mean Δ_p values of 328.59, 298.11, and 221.91 mV for $d_{tx-rx;i}$ equal to 6 cm, 10 cm, and 20 cm distances, respectively.

TABLE III: Pearson correlation between the Δ_p and the d_{tx-rx} and their corresponding p-values.

Experiment	r	p-value
Implantable CC	-0.19	0.53
Implantable GC	-0.88	< 0.01
Wearable CC	-0.28	0.36
Wearable GC	-0.92	< 0.01

TABLE IV: Fitted models in the channel linear regression analysis, including parameter estimates, with their corresponding t-values and p-values for hypothesis testing, besides SW and \bar{R}^2 results.

Experiment	Measure	Model in (12)			Model in (13)		
		Estimate	t-value	p-value	Estimate	t-value	p-value
Implantable CC	\hat{a}	10108.63	12.145	< 0.01	9682.8	22.422	< 0.01
	\hat{b}	-55.40	-0.657	0.52	58.8	0.096	0.92
	\hat{c}				-505.47	-0.717	0.49
	SW	0.90		0.12	0.94		0.47
	\bar{R}^2	-0.05			-0.12		
Implantable GC	\hat{a}	127.99	8.737	< 0.01	79.8	13.494	< 0.01
	\hat{b}	-9.04	-6.097	< 0.01	-54.4	-6.505	< 0.01
	\hat{c}				-68.3	-7.073	< 0.01
	SW	0.96		0.71	0.84		0.02
	\bar{R}^2	0.75			0.84		
Wearable CC	\hat{a}	4518.35	18.663	< 0.01	4388.60	24.110	< 0.01
	\hat{b}	-19.28	-0.958	0.36	-43.40	-0.169	0.87
	\hat{c}				-265.27	-0.892	0.39
	SW	0.84		0.02	0.847		0.03
	\bar{R}^2	-0.01			-0.10		
Wearable GC	\hat{a}	374.31	32.095	< 0.01	324.60	38.304	< 0.01
	\hat{b}	-7.62	-7.852	< 0.01	-20.80	-1.736	0.11
	\hat{c}				-105.27	-7.607	< 0.01
	SW	0.98		0.95	0.94		0.48
	\bar{R}^2	0.84			0.83		

C. Analysis based on noise thresholding and CIR calibration

1) *Noise thresholding*: Additional experiments were conducted considering only the contribution of the main values of the channel impulse response and discarding other noise contributions lower than a suitable threshold. The method estimates the SNR and deletes the contributions of the CIR with values lower than a threshold set equal to $\sqrt{\sigma_n^2}$, where σ_n^2 is the estimated noise variance. Fig. 12 shows results obtained in implantable configurations and compares them with a setting where a cable was used to connect the transmitter and the receiver. In particular, Fig. 12 (a), (b), (c) report the full CIR, while 12 (d), (e), (f) report only the CIR contributions with values higher than the threshold; it can be noticed that the CIR in the setting with the cable presents less samples than the

one with wireless transmission via CC and GC. In particular, the impulse response presents three main samples in the first case, which increase to around ten in the other cases. Similarly, 12 (g), (h), (i) and 12 (j), (k), (l) illustrate the full CFR and the one obtained from the CIR with thresholding, respectively, showing more clearly the flat nature of the channel with higher channel gain for CC than GC technology. In more details, Fig. 12 (j) illustrates the flat channel with cable, while showing its low pass behaviour with around 10 dB major attenuation at higher frequencies. Fig. 12 (k) depicts the high-pass behaviour of the CC channel, with higher attenuation at low frequencies due to the capacitive effect of the body. CF magnitude rises indeed from 36 dB to 80 dB at medium frequencies, to then settle at 65 dB for higher frequencies. A similar, slightly high-pass behaviour is visible for the GC channel in Fig. 12 (l) although with CFR values lower than CC. The low-pass filter effect observed at normalized frequencies above 0.9 is due to anti-aliasing filters in the sound cards.

2) *CIR calibration*: In order to better characterize the measured intra-body CIR, it is possible to equalize both the cable and the complete transceiver device effects using the CIR estimated in direct *tx-to-rx* cable connection conditions, as in Fig. 12.

After removing noise by thresholding, the estimated discrete-time CIR of the cable channel can be written as

$$h_c(n) \equiv R_{xy_c}(n\tau_s) \quad (15)$$

where $R_{xy_c}(\tau)$ represents the estimated CIR when the received signal $y_c(t)$ is collected after a cable that directly connects transmitter and receiver; τ_s is the sampling interval.

Once estimated $h_c(n)$, the intra-body discrete-time CIR $h(n) \equiv R_{xy}(n\tau_s)$ can be equalized by using the following inverse filter, i.e. the zero-forcing (ZF) criterion,

$$\mathbf{W}_c = \left(\mathbf{H}_c \mathbf{H}_c^H \right)^{-1} \quad (16)$$

where \mathbf{W}_c is the convolution matrix corresponding to the inverse ZF filter, while \mathbf{H}_c is the convolution matrix of the discrete-time cable CIR of length L . L is determined after thresholding, by considering only non-zero elements of $h_c(n)$

$$\mathbf{h}_c \equiv [h_c(0), h_c(1), \dots, h_c(L-1)]. \quad (17)$$

In order to better mitigate noise effects, the minimum mean square error (MMSE) criterion can be also used:

$$\mathbf{W}_c = \left(\mathbf{H}_c \mathbf{H}_c^H + \sigma_n^2 \mathbf{I} \right)^{-1} \quad (18)$$

where σ_n^2 is the noise variance defined above.

Our experiments, however, verified that the equalized estimated CIR is practically equivalent to the ones depicted in Fig. 12. This outcome confirms that the cable CIR can be effectively represented by an ideal flat channel that does not affect the measured intra-body CIR when employing CC and GC technologies.

VI. CONCLUSIONS AND FUTURE DIRECTIONS

In this paper, we discussed the characterization of communication channels inside the human body by means of impulse

response measurement, with the aim of comparing CC and GC technologies in both wearable and implantable configurations. Experimental results demonstrate that the tested body channel is relatively flat in the frequency range of interest up to 100 KHz, which makes a simple baseband transceiver design suitable in principle for IBNs. One interesting finding is that implantable CC with isolated ground -not deeply investigated so far- can compete with the more widely used GC, thanks to its ability to cover long distances with very low transmission power. Another important result regards the channel responses and the distance between the transmitter and the receiver. By using linear correlation and regression models, we demonstrated that only GC channels present significant relationships between these variables within the distances under investigation.

Future avenues of development include the investigation of the channel at higher frequencies, up to 100 MHz. This will require a different hardware to replace the currently employed testbed but would also enable comparison with existing experimental results, such as [17] that focused on higher frequencies. Higher frequencies enable broader bandwidths and thus higher data rates, however according to existing studies the channel tends to become frequency-dependent [12], [13], [45], and thus requires more complex and energy-hungry transceivers to counteract its effects. On the contrary, the evaluation in the present work shows a flat channel at low frequencies up to 100 KHz, where simple and low-consumption transceivers may suffice. This feature suits well both the IBC requirement of utilizing low-power devices, and the moderate bandwidth needed for most physiological signals. Furthermore, the impact of own body motion will be evaluated in channel characterization, although from our preliminary analysis we expect the impact to be much smaller than for RF WBAN channels.

Specialized transmission techniques suited for IBC may be designed that leverage the channel model findings; these techniques may include UWB, compressive sensing transmission methods [53], simple-multiple channels [54] and basic digital modulation schemes [55]. Also, multiple-implants scenarios can be conceived, in which it is fundamental to develop opportunistic wake-up methods enabled by location awareness of devices [56], [57] to minimize energy consumption as required in IBNs.

Regarding miniaturization of implanted devices, CC features a key advantage with respect to GC. This latter requires indeed a minimum inter-electrode distance to ensure proper operation. A tiny device would require really close electrodes at the transmitter, however, all the current would flow between those electrodes and secondary currents would become too weak to be detected at the receiver side. By contrast, in implantable CC the isolated ground electrode can be placed extremely close to the other electrode, unlocking higher degrees of device miniaturization. This feature, together with the experimental results of the channel, suggests that implantable CC is a promising technology in this exciting IBC research area.

REFERENCES

- [1] Y. Lu, R. Ni, and Q. Zhu, "Wireless communication in nanonetworks: Current status, prospect and challenges," *IEEE Transactions on Molec-*

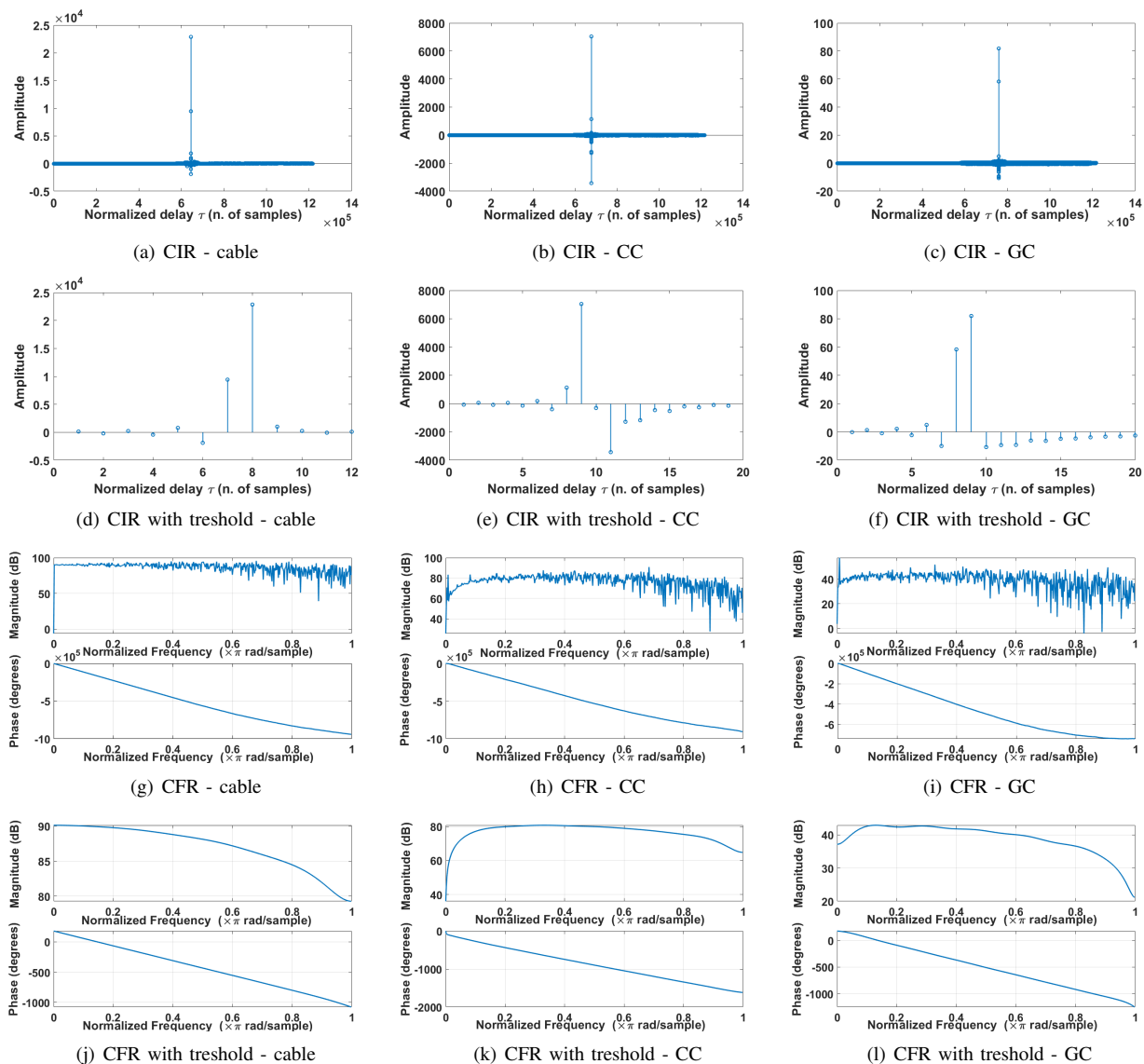


Fig. 12: The measured channel impulse response (CIR) and channel frequency response (CFR) when the received signal is filtered with a thresholding procedure based on SNR and noise variance to remove noise, under three configurations: (i) a cable connecting transmitter and receiver; (ii) CC implanted scenario in *ex-vivo* tissue with 0.5 mm electrodes size and $d_{TX-RX} = 6$ cm, (iii) GC implanted scenario in *ex-vivo* tissue with 0.5 mm electrodes size and $d_{TX-RX} = 6$ cm.

ular, *Biological and Multi-Scale Communications*, vol. 6, no. 2, pp. 71–80, 2020.

[2] R. Dwivedi, D. Mehrotra, and S. Chandra, “Potential of internet of medical things (iomt) applications in building a smart healthcare system: A systematic review,” *Journal of oral biology and craniofacial research*, 2021.

[3] J. Srivastava, S. Routray, S. Ahmad, and M. M. Waris, “Internet of medical things (iomt)-based smart healthcare system: Trends and progress,” *Computational Intelligence and Neuroscience*, vol. 2022, 2022.

[4] W. J. Tomlinson, S. Banou, S. Blechinger-Slocum, C. Yu, and K. R. Chowdhury, “Body-guided galvanic coupling communication for secure biometric data,” *IEEE Transactions on Wireless Communications*, vol. 18, no. 8, pp. 4143–4156, 2019.

[5] S. Banou, M. Swaminathan, G. Reus Muns, D. Duong, F. Kulsoom, P. Savazzi, A. Vizziello, and K. R. Chowdhury, “Beamforming galvanic coupling signals for iomt implant-to-relay communication,” *IEEE Sensors Journal*, vol. 19, no. 19, pp. 8487–8501, 2019.

[6] R. Cavallari, F. Martelli, R. Rosini, C. Buratti, and R. Verdone, “A survey on wireless body area networks: Technologies and design challenges,” *IEEE Communications Surveys & Tutorials*, vol. 16, no. 3, pp. 1635–

1657, 2014.

[7] W. J. Tomlinson, S. Banou, C. Yu, M. Stojanovic, and K. R. Chowdhury, “Comprehensive survey of galvanic coupling and alternative intrabody communication technologies,” *IEEE Communications Surveys & Tutorials*, vol. 21, no. 2, pp. 1145–1164, 2019.

[8] L. Galluccio, S. Milardo, and E. Sciacca, “A feasibility analysis on the use of ultrasonic multihop communications for e-health applications,” in *2017 IEEE International Conference on Communications (ICC)*, 2017, pp. 1–6.

[9] M. Seyed, B. Kibret, D. T. H. Lai, and M. Faulkner, “A survey on intrabody communications for body area network applications,” *IEEE Transactions on Biomedical Engineering*, vol. 60, no. 8, pp. 2067–2079, 2013.

[10] “Ieee standard for local and metropolitan area networks—part 15.6: Wireless body area networks, ieee standard 802.15.6, 2012,” 2012.

[11] L. Vasić, M. Cifrek, Y. Gao, and M. Du, “Preliminary characterization of capacitive intrabody communication channel under implantable-like conditions,” in *2020 IEEE International Instrumentation and Measurement Technology Conference (I2MTC)*, 2020, pp. 1–5.

[12] M. Li, Y. Song, Y. Hou, N. Li, Y. Jiang, M. Sulaman, and Q. Hao,

- “Comparable investigation of characteristics for implant intra-body communication based on galvanic and capacitive coupling,” *IEEE Transactions on Biomedical Circuits and Systems*, vol. 13, no. 6, pp. 1747–1758, 2019.
- [13] J. W. Li, X. M. Chen, B. D. Sekar, C. T. Lam, M. Du, P. U. Mak, M. I. Vai, Y. M. Gao, and S. H. Pun, “Channel characteristics analysis of galvanic coupling intra-body communication,” *IEEE Journal of Electromagnetics, RF and Microwaves in Medicine and Biology*, vol. 6, no. 3, pp. 364–372, 2022.
- [14] M. A. Callejón, D. Naranjo-Hernandez, J. Reina-Tosina, and L. M. Roa, “Distributed circuit modeling of galvanic and capacitive coupling for intrabody communication,” *IEEE Transactions on Biomedical Engineering*, vol. 59, no. 11, pp. 3263–3269, 2012.
- [15] M. Swaminathan, F. S. Cabrera, J. S. Pujol, U. Muncuk, G. Schirmer, and K. R. Chowdhury, “Multi-path model and sensitivity analysis for galvanic coupled intra-body communication through layered tissue,” *IEEE Transactions on Biomedical Circuits and Systems*, vol. 10, no. 2, pp. 339–351, 2016.
- [16] M. A. Callejón, J. Reina-Tosina, D. Naranjo-Hernández, and L. M. Roa, “Galvanic coupling transmission in intrabody communication: A finite element approach,” *IEEE Transactions on Biomedical Engineering*, vol. 61, no. 3, pp. 775–783, 2014.
- [17] W. J. Tomlinson, F. Abarca, K. R. Chowdhury, M. Stojanovic, and C. Yu, “Experimental assessment of human-body-like tissue as a communication channel for galvanic coupling,” in *2015 IEEE 12th International Conference on Wearable and Implantable Body Sensor Networks (BSN)*, 2015, pp. 1–6.
- [18] P. Papazian and J. Lemmon, “Radio channel impulse response measurement and analysis,” 2011.
- [19] E. C. Sciacca and L. Galluccio, “Impulse response analysis of an ultrasonic human body channel,” *Computer Networks*, vol. 171, p. 107149, 2020.
- [20] J. H. Hwang, T. W. Kang, S. O. Park, and Y. T. Kim, “Empirical channel model for human body communication,” *IEEE Antennas and Wireless Propagation Letters*, vol. 14, pp. 694–697, 2015.
- [21] J.-H. Hwang, T.-W. Kang, Y.-T. Kim, and S.-O. Park, “Measurement of transmission properties of hbc channel and its impulse response model,” *IEEE Transactions on Instrumentation and Measurement*, vol. 65, no. 1, pp. 177–188, 2016.
- [22] T. Kang, K.-I. Oh, J.-H. Hwang, S. Kim, H. Park, and J. Lee, “Measurement and analysis of electric signal transmission using human body as medium for wlan applications,” *IEEE Transactions on Instrumentation and Measurement*, vol. 67, no. 3, pp. 527–537, 2018.
- [23] T. Kang, S. Kim, K.-I. Oh, J.-H. Hwang, J. Lee, H. Park, K. Byun, and W. Lee, “Evaluation of human body characteristics for electric signal transmission based on measured body impulse response,” *IEEE Transactions on Instrumentation and Measurement*, vol. 69, no. 9, pp. 6399–6411, 2020.
- [24] A. Vizziello, P. Savazzi, and F. Dell’Acqua, “Data driven channel characterization of human body communication,” in *Proceedings of the 9th ACM International Conference on Nanoscale Computing and Communication*, ser. NANOCOM ’22. New York, NY, USA: Association for Computing Machinery, 2022. [Online]. Available: <https://doi.org/10.1145/3558583.3558869>
- [25] A. Vizziello, P. Savazzi, and G. Magenes, “Electromyography data transmission via galvanic coupling intra-body communication link,” in *Proceedings of the Eight Annual ACM International Conference on Nanoscale Computing and Communication*, ser. NANOCOM ’21. New York, NY, USA: Association for Computing Machinery, 2021. [Online]. Available: <https://doi.org/10.1145/3477206.3477450>
- [26] P. K. B. Rangaiah, M. Kouki, Y. Dhoubi, F. Huss, B. Mandal, B. Augustine, M. D. Perez, and R. Augustine, “Dielectric characterization and statistical analysis of ex-vivo burnt human skin samples for microwave sensor development,” *IEEE Access*, vol. 11, pp. 4359–4372, 2023.
- [27] A. Vizziello, M. Magarini, P. Savazzi, and L. Galluccio, “Intra-body communications for nervous system applications: Current technologies and future directions,” *Computer Networks*, vol. 227, p. 109718, 2023.
- [28] P. Vecchia, R. Matthes, G. Z. J. Lin, R. Saunders, and A. Swerdlow, *Exposure to high frequency electromagnetic fields, biological effects and health consequences (100kHz-300 GHz)*. International Commission on Non-Ionizing Radiation Protection, 2009.
- [29] D. Naranjo-Hernández, A. Callejón-Leblic, Z. Lucev, M. Seyedi, and Y. Gao, “Past results, present trends, and future challenges in intrabody communication,” *Wirel. Commun. Mob. Comput.*, vol. 2018, 2018.
- [30] M. Swaminathan, A. Vizziello, D. Duong, P. Savazzi, and K. R. Chowdhury, “Beamforming in the body: Energy-efficient and collision-free communication for implants,” in *IEEE INFOCOM 2017 - IEEE Conference on Computer Communications*, 2017, pp. 1–9.
- [31] K. Zhang, Q. Hao, Y. Song, J. Wang, R. Huang, and Y. Liu, “Modeling and characterization of the implant intra-body communication based on capacitive coupling using a transfer function method,” *Sensors (Basel)*, vol. 4, no. 1, pp. 1740–56, 2014.
- [32] M. Li, Y. Song, G. Wang, Q. Hao, and K. Zang, “Characterization of the implantable intra-body communication based on capacitive coupling by transfer function,” in *2016 10th International Conference on Sensing Technology (ICST)*, 2016, pp. 1–5.
- [33] A. F. Molisch, *Channel Sounding*, 2011, pp. 145–164.
- [34] R. Plonsey and D. B. Heppner, “Considerations of quasi-stationarity in electrophysiological system,” *Bulletin of Mathematical Biophysics*, vol. 29, p. 657–664, 19673.
- [35] M. Varela and M. Sanchez, “Rms delay and coherence bandwidth measurements in indoor radio channels in the uhf band,” *IEEE Transactions on Vehicular Technology*, vol. 50, no. 2, pp. 515–525, 2001.
- [36] D. C. Montgomery, E. A. Peck, and G. G. Vining, *Introduction to linear regression analysis*. John Wiley & Sons, 2021.
- [37] S. S. Shapiro and M. B. Wilk, “An analysis of variance test for normality (complete samples),” *Biometrika*, vol. 52, no. 3/4, pp. 591–611, 1965.
- [38] A. Vizziello, P. Savazzi, G. Magenes, and P. Gamba, “Phy design and implementation of a galvanic coupling testbed for intra-body communication links,” *IEEE Access*, vol. 8, pp. 184 585–184 597, 2020.
- [39] A. Vizziello and P. Savazzi, “Code of sound card-based testbed for an intra-body galvanic coupling link,” 2020. [Online]. Available: <https://doi.org/10.24433/CO.7879297.v1>
- [40] M. A. Callejón, J. Reina-Tosina, D. Naranjo-Hernández, and L. M. Roa, “Measurement issues in galvanic intrabody communication: Influence of experimental setup,” *IEEE Transactions on Biomedical Engineering*, vol. 62, no. 11, pp. 2724–2732, 2015.
- [41] C. Gabriel, S. Gabriel, and E. Corthout, “The dielectric properties of biological tissues: I. Literature survey,” *Phys Med Biol*, vol. 41, pp. 2231–49, 1996.
- [42] D. Vasisht, G. Zhang, O. Abari, H.-M. Lu, J. Flanz, and D. Katabi, “In-Body Backscatter Communication and Localization,” in *Proceedings of the 2018 Conference of the ACM Special Interest Group on Data Communication*, ser. SIGCOMM ’18. New York, NY, USA: Association for Computing Machinery, 2018, p. 132–146.
- [43] M. V. Traffano-Schiffo, M. Castro-Giraldez, R. J. Colom, P. Talens, and P. J. Fito, “New methodology to analyze the dielectric properties in radio frequency and microwave ranges in chicken meat during postmortem time,” *Journal of Food Engineering*, vol. 292, p. 110350, 2021.
- [44] H. Kanai, I. Chatterjee, and O. Gandhi, “Human body impedance for electromagnetic hazard analysis in the vlf to mf band,” *IEEE Transactions on Microwave Theory and Techniques*, vol. 32, no. 8, pp. 763–772, 1984.
- [45] M. A. Callejón, D. Naranjo-Hernández, J. Reina-Tosina, and L. M. Roa, “A comprehensive study into intrabody communication measurements,” *IEEE Transactions on Instrumentation and Measurement*, vol. 62, no. 9, pp. 2446–2455, 2013.
- [46] T. C. W. Schenk, N. S. Mazloum, L. Tan, and P. Rutten, “Experimental characterization of the body-coupled communications channel,” in *2008 IEEE International Symposium on Wireless Communication Systems*, 2008, pp. 234–239.
- [47] N. Cho, J. Yoo, S.-J. Song, J. Lee, S. Jeon, and H.-J. Yoo, “The human body characteristics as a signal transmission medium for intrabody communication,” *IEEE Transactions on Microwave Theory and Techniques*, vol. 55, no. 5, pp. 1080–1086, 2007.
- [48] J. Ruiz, J. Xu, and S. Shimamoto, “Propagation characteristics of intra-body communications for body area networks,” in *CCNC 2006. 2006 3rd IEEE Consumer Communications and Networking Conference, 2006.*, vol. 1, 2006, pp. 509–513.
- [49] J. A. Ruiz and S. Shimamoto, “Statistical modeling of intra-body propagation channel,” in *2007 IEEE Wireless Communications and Networking Conference*, 2007, pp. 2063–2068.
- [50] R. Xu, W. C. Ng, H. Zhu, H. Shan, and J. Yuan, “Equation environment coupling and interference on the electric-field intrabody communication channel,” *IEEE Transactions on Biomedical Engineering*, vol. 59, no. 7, pp. 2051–2059, 2012.
- [51] Z. Nie, J. Ma, Z. Li, H. Chen, and L. Wang, “Dynamic propagation channel characterization and modeling for human body communication,” *Sensors*, vol. 12, no. 12, pp. 17 569–17 587, 2012. [Online]. Available: <https://www.mdpi.com/1424-8220/12/12/17569>
- [52] W. Sun, J. Zhao, Y. Huang, Y. Sun, H. Yang, and Y. Liu, “Dynamic channel modeling and ofdm system analysis for capacitive coupling body

- channel communication," *IEEE Transactions on Biomedical Circuits and Systems*, vol. 13, no. 4, pp. 735–745, 2019.
- [53] F. Kulsoom, A. Vizziello, H. N. Chaudhry, and P. Savazzi, "Pilot reduction techniques for sparse channel estimation in massive mimo systems," in *2018 14th Annual Conference on Wireless On-demand Network Systems and Services (WONS)*, 2018, pp. 111–116.
- [54] F. Kulsoom, A. Vizziello, R. Borra, and P. Savazzi, "Reduced complexity kalman filtering for phase recovery in xpic systems," *Physical Communication*, vol. 29, pp. 112–119, 2018.
- [55] C. Zhang, Q. Jin, M. Zhao, D. Zhang, and L. Lin, "An experimental study of digital communication system with human body as communication channel," in *2022 IEEE-EMBS International Conference on Wearable and Implantable Body Sensor Networks (BSN)*, 2022, pp. 1–4.
- [56] S. Kianoush and et al, "Energy-efficient and mobile-aided cooperative localization in cognitive radio networks," *IEEE Transactions on Vehicular Technology*, vol. 65, no. 5, pp. 3450–3461, 2016.
- [57] M. Stelzner and I. Traupe, "Fcnn: Location awareness based on a lightweight hop count routing body coordinates concept," in *Proceedings of the Sixth Annual ACM International Conference on Nanoscale Computing and Communication*, ser. NANOCOM '19. New York, NY, USA: Association for Computing Machinery, 2019.